Supplementary Material

Overcoming Non-Radiative Losses with AlGaAs PIN Junctions for Near-Field Thermophotonic Energy Harvesting

Julien Legendre and Pierre-Olivier Chapuis

Univ Lyon, CNRS, INSA-Lyon, Université Claude Bernard Lyon 1, CETHIL UMR5008, F-69621, Villeurbanne, France

Contents

I. Comparison with performances of other devices

In order to highlight the benefit of using near-field thermophotonics (NF-TPX) compared to other technologies, we show in Fig. (S1) the variation of the power produced as a function of the hot source temperature for thermoelectrics (TE), thermophotovoltaics (TPV), near-field thermophotovoltaics (NF-TPV) and NF-TPX. The calculations performed are inspired by those of Okanimba Tedah et al. [1], with slightly different parameters. The models and values used are described in subsections (I A) to (I C) below. One main difference is that we

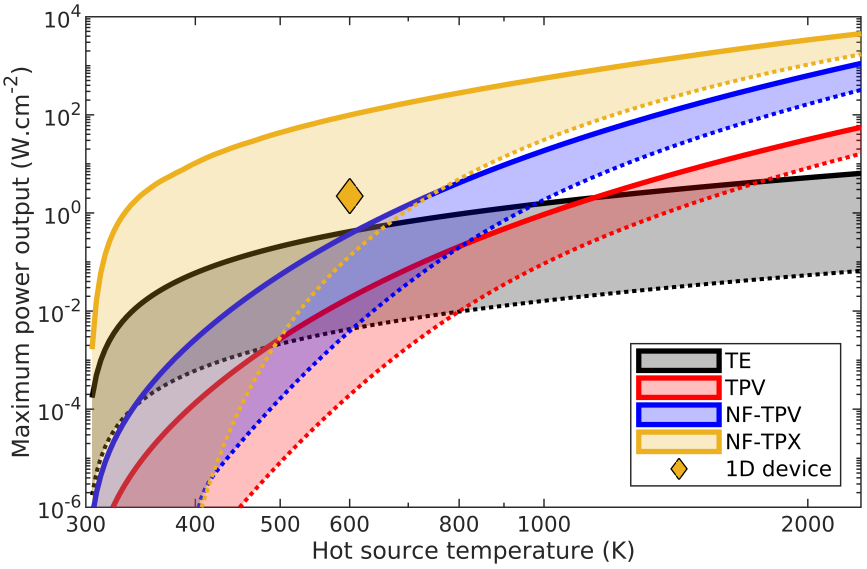

FIG. S1. Variation of the power output of different devices with the hot source temperature.

consider both bodies to be at constant temperature. Therefore, thermal management issues causing a decrease of performance at high hot source temperature cannot be observed here.

As mentioned in the core article, TPV can hardly compete against TE below 1000 K, while going to the near field allows to perform well down to 700 K. For NF-TPX, capabilities at low temperature are harder to predict: while the upper bound is orders of magnitude higher than for TE, the lower bound is orders of magnitude lower at very low temperatures, and is then barely better than TPV. Compared to the ideal case, the power output drops by a factor 10^7 at 400 K, 10^4 at 500 K, 10^3 at 600 K for an IQE (0.9) much higher than the one used for the lower bound of TPV (10^{-4}). The large range of possible power outputs at low temperatures is, as explained in the article, related to the large impact of the LED IQE on the performance, which must be close to 1 in order to reach the electroluminescent cooling regime. While for TPV the device is able to produce power at any IQE, TPX devices stop working below a certain value and are thus much more sensitive to it.

Here, IQE is defined in a similar fashion to that of the article, i.e. as the fraction of recombinations being radiative. This corresponds to the usual definition of the IQE for an LED, but is quite different from its PV cell counterpart (which focuses on the incoming photon conversion efficiency). This 'LED' IQE has much lower impact on the PV cell than on the LED: this is the reason why the IQE used for TPV is so low. In addition, it should be kept in mind that while the influence of the IQE becomes lower at higher temperature,

it gets harder and harder to reach high IQE at these temperatures. Moreover, thermal management issues starts to be critical both in the LED and the PV cell. We have chosen to plot NF-TPX performance up to the LED melting temperature (between 1500 K and 2000 K for AlGaAs, depending on the Al fraction), which is certainly well above realistic maximum temperature. In practice, NF-TPX devices are envisioned at low temperature.

Despite the strong effect of the LED IQE, NF-TPX can be promising for low-grade heat recovery. For an IQE of 0.9, it starts to be competitive against TE above 500 K, and any gain on the LED IQE will significantly rise the power output. The 1D case considered in the article, corresponding to the diamond in the figure, shows better performance than any other technology (even at upper bound) at 600 K, with a factor 5 enhancement compared to TE. This enhancement factor goes up to 6 and 120 for NF-TPV and TPV, respectively.

A. Thermoelectrics

We use the expression of the maximum power given by Apertet et al. [2]:

$$P_{max} = G_{contact} \frac{Z\bar{T}}{\left(1+\sqrt{1+Z\bar{T}}\right)^2} \frac{\Delta T^2}{4\bar{T}} \tag{S1}$$

For the lower (resp. higher) limit, we choose $Z\bar{T} = 1$ (resp 3) - corresponding to available and ambitious cases - and $G_{contact} = 5$ W.m^{-2}.K^{-1} (resp. $G_{contact} = 250$ W.m^{-2}.K^{-1}), which are the values used by Okanimba Tedah et al. [1].

B. Thermophotovoltaics and near-field thermophotovoltaics

We consider that the PV cell is kept at constant temperature to be consistent with NF-TPX calculations. We assume blackbody radiation between the emitter (body 1) and the PV cell (body 2) in the case of far-field TPV. Without any non-radiative losses (upper limit) we have:

$$\begin{aligned} P = U \cdot J(U) &= eU \cdot \gamma_{12,a} \\ &= eU \cdot \frac{\hbar}{4\pi^2 c^2} \int_{E_g}^{\infty} \Delta n_{12}^0(\omega) \cdot \omega^3 d\omega \end{aligned} \tag{S2}$$

If non-radiative losses are added through a flat IQE (which is the ratio between radiative

recombinations and total recombinations), this becomes:

$$P = U \cdot J(U) = eU \cdot \left(\gamma_{12,a} - \frac{1 - IQE}{IQE} (\gamma_{2,a}^{U} - \gamma_{2,a}^{0}) \right) \tag{S3a}$$

$$\gamma_{2,a}^{U} = \frac{\hbar}{4\pi^2 c^2} \int_{E_g}^{\infty} n_2^0(\omega, eU, T_2) \cdot \omega^3 d\omega \tag{S3b}$$

In this case, we have used $E_g = 0.354$ eV, corresponding to the bandgap of InAs. This low bandgap allows to obtain good capabilities at moderate emitter temperature. For the lower bound, we use IQE of 10^{-4}, which allows to obtain a power output similar to that of Milovich et al. [3] in the far-field at 800 K.

For the near-field effects, we assume a simple enhancement factor equal to 20 compared to the far-field value. This factor corresponds to the increase of the above-bandgap heat flux at 10 nm gap distance. To compute this, we considered similar input data to those of Milovich et al. except for the InAs dielectric function [4]. Note that for a 100 nm gap distance, they obtained a $\times 30$ power enhancement factor. A more complete calculation, including charge carrier transport, would be required to have a better estimation of this factor at 10 nm.

C. Near-field thermophotonics

A similar description to the one used for TPV is applied for NF-TPX. Both the LED (body 1) and the PV cell (body 2) are still considered semi-infinite. However, we use AlGaAs and GaAs (therefore no longer radiating at the blackbody limit), and the near-field effects are precisely computed at a distance of 10 nm - in a equivalent manner to the 1D resolution introduced in the article.

The expressions obtained are similar to Eq. (S2) and (S3a), except that they should be computed both for the LED and the PV cell. Without any non-radiative recombinations (upper limit), it gives back the '0D ideal case' used in the article. The lower limit is obtained for a flat IQE of 0.9 applied to the LED and the PV cell. As previously explained, this only has a small influence on the PV cell performance, and mainly has an effect on the LED.

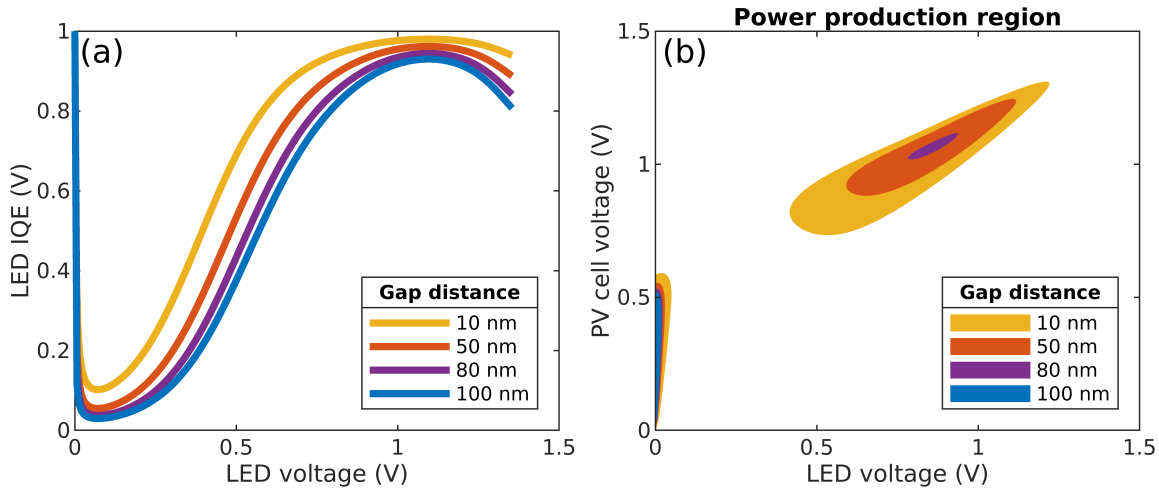

FIG. S2. Variation of (a) the LED IQE (at null PV cell voltage), (b) the device full characteristic with the gap distance.

II. Zoom on the variation of the device performance with the gap distance

We aim at giving more insight on the sudden drop of power output when the gap distance is increased up to 100 nm (shown in Fig. (4) of the article). As seen in Fig. (S2a), increasing d lowers the LED IQE. This happens mainly because the radiative term of Eq. (8a) in the article is decreasing at a higher rate than the non-radiative term. This drop is larger in the transition region between low and high IQEs, reaching 30% in absolute value at 0.5 V. While the decrease is lower at higher voltage (5 to 15%), this is enough to largely reduce the power production region (PPR), as shown in Fig. (S2b). With this figure, the brutal change of performance with distance becomes clearer: up to 80 nm, a PPR still exists at high voltage, making the variation of power output relatively smooth. However, between 80 nm and 100 nm gap distance, the wall-plug efficiency (WPE) becomes too low and only the close-to-TPV PPR remains (close to the y-axis), in which the power output is low. It is interesting to notice that while the maximum LED IQE is always reached at a LED voltage close to 1.1 V, the PPR is actually centered around 0.9 V. Since the PPR is related to energy balance (rather than carriers), quantities such as the LED WPE or the PV cell efficiency are better metrics to predict its position. For instance, for a 80 nm gap distance and a 1.1 V PV cell voltage, the WPE reaches a maximum close to an LED voltage of 0.83 V. The PV cell being more efficient under higher radiative heat flux (i.e., at higher LED voltage), the

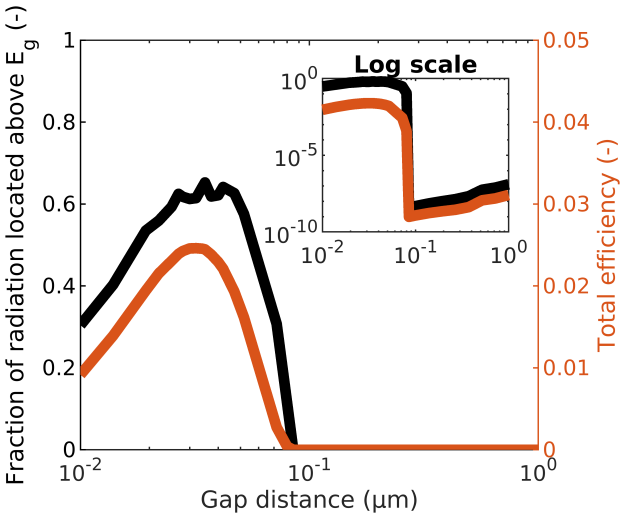

FIG. S3. Variation of the fraction of radiation located above the bandgap (left axis) and of the total efficiency (right axis) as a function of the gap distance.

optimum LED voltage is obtained as a trade-off between the LED and PV cell efficiencies and is located close to 0.9 V.

To complete the discussion about the fraction of radiation located above the bandgap α discussed in the main article, we show its variation with the gap distance along with the total efficiency in Fig. (S3). This makes the correlation between the two quantities quite clear. A maximum is found between 30 and 40 nm, with a close-to-logarithmic decrease further away from this region. The small oscillations of α, which can be seen around the maximum, are probably due to cavity effect. Such features can also be seen on the above-bandgap heat flux in Fig. (4a) of the main article, although less visible than in Fig. (S3).

III. Details of the charge carrier modelling

A. Numerical model

As stated in the core article, we iteratively solve Poisson, continuity and drift-diffusion equations. To do so, we use the so-called Slotboom variables Φ_n, Φ_p [5] and the normalised electrostatic potential Ψ. The carrier concentrations are then expressed as

$$n = n_i \exp\left(\frac{eV}{k_b T}\right) \exp\left(-\frac{E_{Fn}}{k_b T}\right) = n_i \exp\left(+\Psi\right)\Phi_n, \tag{S4a}$$

$$p = n_i \exp\left(-\frac{eV}{k_b T}\right) \exp\left(\frac{E_{Fp}}{k_b T}\right) = n_i \exp\left(-\Psi\right)\Phi_p, \tag{S4b}$$

where E_{Fn}, E_{Fp} are the associated quasi-Fermi levels and V is the electrostatic potential. This allows to express the system of equations as follows:

$$\frac{d^2\Psi}{d\bar{z}^2}(z) = (\exp\left(\Psi(z)\right)\Phi_n(z) - \exp\left(-\Psi(z)\right)\Phi_p(z) + N(\,z)), \tag{S5}$$

$$J_n(z) = +e \cdot n_i D_n \exp\left(+\Psi(z)\right) \cdot \frac{d\Phi_n}{dz}(z) = a_n(\Psi(z))\frac{d\Phi_n}{dz}(z), \tag{S6a}$$

$$J_p(z) = -e \cdot n_i D_p \exp\left(-\Psi(z)\right) \cdot \frac{d\Phi_p}{dz}(z) = a_p(\Psi(z))\frac{d\Phi_p}{dz}(z), \tag{S6b}$$

$$\frac{dJ_n}{dz}(z) = +e(R(z) - G(z)), \tag{S7a}$$

$$\frac{dJ_p}{dz}(z) = -e(R(z) - G(z)). \tag{S7b}$$

N corresponds to the doping level, and is negative for donors, while $\bar{z}$ is the position normalised by the Debye length. The general resolution method has been explained in several articles or textbooks [6, 7]. Solving alternatively Poisson equation (to obtain Ψ) and continuity and drift-diffusion equations (to obtain Φ_n and Φ_p) using the previous solution as input for unknown quantities, we are able to obtain self-consistent solutions. Poisson equation is solved using linearisation and an iterative process.

Regarding the resolution of continuity and drift-diffusion equations, several methods can be used [8–10]. In our case, we choose to solve them via integration to reduce the risk of numerical instability. To do so, we first compute the electron and hole currents using continuity equations and the value given by the recombination current at one of the interfaces, which gives for instance for electrons:

$$J_n(z) = J_n(z_b) + e\int_{z_b}^{z}(R(z') - G(z'))dz'. \tag{S8}$$

Then, the Slotboom variables are obtained using drift-diffusion equations and the condi-

tion of equilibrium at contacts for majority carriers (which gives Φ at one of the interfaces), e.g. for electrons:

$$\Phi_n(z) = \Phi_n(z_b) + \int_{z_b}^{z} \frac{J_n(z')}{a_n(\Psi(z'))} dz'. \tag{S9}$$

In order to help convergence, after each iteration in which we solve the whole system, the obtained solution is averaged with the previous one using specific weights. We verified that such process did not change the final solution.

B. Comparison with low-injection approximation

In order to show the interest of solving fully the system of equations rather than using approximations (as in our previous article [11]), we compare our results with those obtained with the low-injection approximation (LIA). To simplify the study, we do this comparison only on Shockley-Read-Hall (SRH) recombination rates. In the LIA, the doping level is supposed to be high enough so that the majority carrier density is constant in the layer. For instance, for n-doped layers, the SRH expression given in Eq. (8a) of the main article becomes:

$$R_{SRH}(z) = \frac{(N_d p - n_i^2)}{\tau_p N_d} = \frac{\Delta p}{\tau_p}, \tag{S10}$$

where Δp corresponds to the difference of hole density compared to equilibrium.

We consider the same cases as the ones shown in Fig. (3) of the main article (i.e. with only one component being biased) using the charge carrier densities obtained after convergence of the complete model (shown in Fig. (S4)). The results obtained are represented in Fig. (S5). The LIA works well in the highly doped regions (at the boundaries of the junctions), even if it starts to diverge for the LED at high voltage due to large photon emission. In the intrinsic region however, it becomes erroneous and can be off by orders of magnitude compared to the complete resolution. This is due to the electron density deviating from $N_d = 10^{16}$ cm^{-3}. Expressions such as Eq. (S10) thus cannot be used for PIN junctions. When using the LIA, the depleted layer is often resolved analytically to prevent such issue; however, this is not possible here, since the PI and IN junctions overlap each other. For instance it can be observed that in the LED, at low voltage, the electron concentration does not stabilise to N_d in the intrinsic layer (while it does in the three other cases).

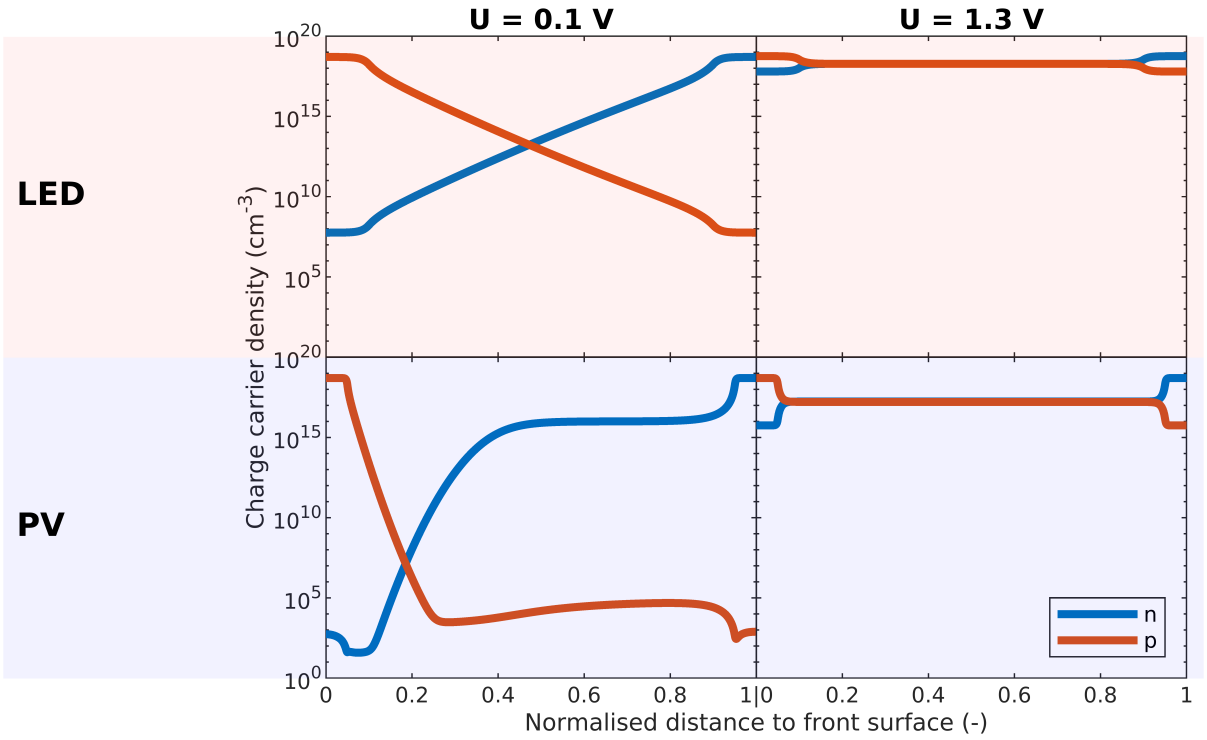

FIG. S4. Charge carrier densities in the LED and in the PV cell at different voltages with the opposite component kept at 0 V.

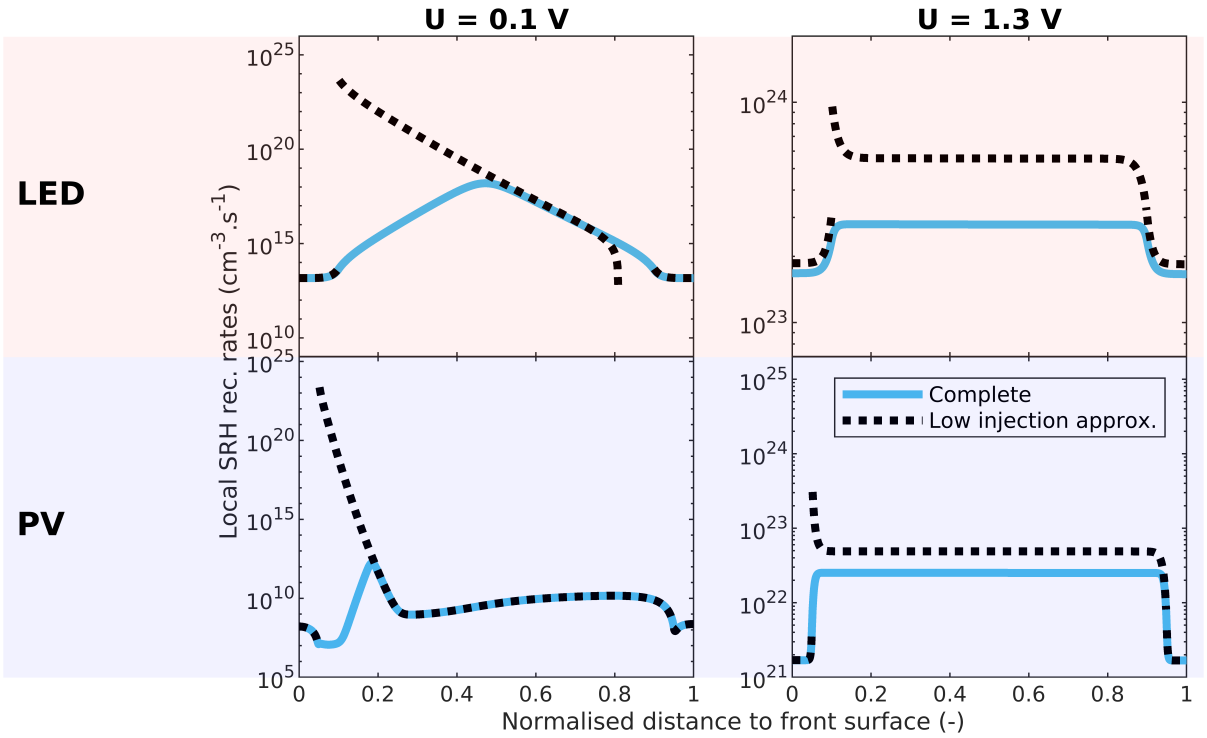

FIG. S5. Comparison of SRH recombination rates obtained with the charge carrier densities shown in Fig. (S4), with the complete expression or with the low-injection approximation. The study is performed for the LED and the PV cell while the opposite component is unbiased.

[1] I. A. Okanimba Tedah, F. Maculewicz, D. E. Wolf, and R. Schmechel, Journal of Physics D: Applied Physics **52**, 275501 (2019).

[2] Y. Apertet, H. Ouerdane, O. Glavatskaya, C. Goupil, and P. Lecoeur, EPL (Europhysics Letters) **97**, 28001 (2012).

[3] D. Milovich, J. Villa, E. Antolin, A. Datas, A. Marti, R. Vaillon, and M. Francoeur, Journal of Photonics for Energy **10**, 025503 (2020).

[4] S. Adachi, Journal of Applied Physics **66**, 6030 (1989).

[5] J. W. Slotboom, IEEE Transactions on Electron Devices **20**, 669 (1973).

[6] H. K. Gummel, IEEE Transactions on Electron Devices **11**, 455 (1964).

[7] D. Vasileska, S. M. Goodnick, and G. Klimeck, *Computational Electronics: Semiclassical and Quantum Device Modeling and Simulation* (CRC Press, 2017).

[8] D. L. Scharfetter and H. K. Gummel, IEEE Transactions on Electron Devices **16**, 64 (1969).

[9] E. Blandre, *Thermal radiation at the nanoscale: near-field and interference effects in few-layer structures and on the electrical performances*, Ph.D. thesis, Université de Lyon (2016).

[10] E. Blandre, P.-O. Chapuis, and R. Vaillon, Scientific Reports **7**, 15860 (2017).

[11] J. Legendre and P.-O. Chapuis, Solar Energy Materials and Solar Cells **238**, 111594 (2022).